International Forum on Aeroelasticity and Structural Dynamics
IFASD 2019
9-13 June 2019, Savannah, Georgia, USA

ANALYSIS OF LIGHT DYNAMIC STALL USING DYNAMIC MODE DECOMPOSITION – IFASD 2019-036

Wrik Mallik[1] **and Daniella E. Raveh**[1]

[1]Department of Aerospace Engineering, Technion - IIT
Haifa 3200003, Israel
wrik.mallik@technion.ac.il
daniella@technion.ac.il

Keywords: Dynamic stall, Dynamic Mode Decomposition

Abstract: This study presents an analysis of dynamic stall using dynamic modal decomposition (DMD). The hybrid, delayed detached eddy simulations, with a $k-\omega$ SST turbulence model, were employed to perform the dynamic stall simulations for a pitching NACA 0012 airfoil, at a Mach number of 0.3 and a Reynolds number of 4×10^6. With a mean angle of attack of 11° and peak pitching amplitude of 5°, the dynamic stall observed here can be considered to be in the light stall regime, where potential energy transfer from the flow to the airfoil's motion is often observed. DMD analysis of the pressure snapshots was performed to investigate the modal behavior representing the various physical phenomena of light stall at high, turbulent Reynolds number. The stochastic nature of the turbulent dynamic stall phenomenon was also investigated by comparing the DMD pressure modes from various cycles of the pitching airfoil motion to the phase-averaged DMD pressure modes.

NOMENCLATURE

c	=	Chord
cl	=	Lift coefficient
$cm_{y,x/c=0.25}$	=	Pitching moment coefficient at quarter-chord
cp	=	Pressure coefficient
$\bar{f}$	=	Reduced frequency, $\bar{f} = \frac{\omega c}{2V_\infty}$
t	=	Time
t	=	Nondimensional time, $t_{nd} = t\, V_\infty / c\, M_\infty$
M	=	Mach number
N	=	Number of snapshots
V_∞	=	Freestream velocity
α_0	=	Mean angle of attack
α_1	=	Amplitude of pitching
ω	=	Frequency (rad/sec)

1 INTRODUCTION

Dynamic stall is a complex fluid dynamics phenomenon that manifests itself during rapid, transient motion in which the angle of incidence surpasses the static stall limit. It has been an active area of research for helicopters, wind turbine blades, unmanned aerial vehicle (UAV) and micro aerial vehicle (MAV) applications, as well as low-Reynolds number insect and flapping-wing bird flight. Dynamic stall can be separated into a light stall and a deep stall regime. In light dynamic stall regime, the excursion of the peak dynamic angle of attack from the static stall angle is smaller than the deep dynamic stall regime, leading to less abrupt drop in the lift and moment coefficients during dynamic stall in the light stall regime [1, 2].

The inherent complexity and flow separation during dynamic stall phenomenon require high-fidelity computational fluid dynamic (CFD) simulations for accurate analysis. The choice of governing equations to be solved numerically is important. While several studies in the past have used the Reynolds Averaged Navier Stokes (RANS) equations for studying dynamic stall [3–6], RANS may be susceptible to inaccuracies in presence of strong separation. An alternative is to use Large Eddy Simulations (LES) in which the smaller turbulent length scales are modeled and the larger ones are resolved [7, 8]. However, owing to the large computational cost associated with LES, hybrid RANS/LES methods capable of representing a RANS-type behavior in the vicinity of the solid boundary and an LES-type behavior far away from the wall boundary, have also been used extensively [9].

Modal decomposition of dynamic phenomena often leads to key insight into the physics of the problem. This has led to the application of techniques like proper orthogonal decomposition (POD) [10] and dynamic mode decomposition (DMD) [11] for studying various complex dynamic physical phenomena. DMD is a data-based technique that extracts dominant dynamic features from time-resolved measurements of the flow-field, but unlike POD, the DMD modes also have associated damping, thus indicating the stability of the modes. Computation of modal damping during light dynamic stall is important as energy transfer from the flow to the airfoil oscillations can occur in this stall regime. Such energy transfer can lead to stall flutter instabilities in an associated aeroelastic system.

DMD has been used recently for analyzing both deep dynamic stall simulations with RANS [12] and LES [13], as well as dynamic stall experiments [14]. However, in these studies, the deep dynamic stall regime was generally explored at low to moderate, transitional Reynolds numbers. Thus, the light dynamic stall regime at high, turbulent Reynolds number, where many UAVs operate, has not been explored comprehensively. In the present study, DMD will be used to analyze computational, time-resolved simulations of light dynamic stall at high Reynolds number, where the flow can be considered to be fully turbulent. A RANS-LES hybrid, delayed detached eddy simulations (DDES), with a $k-\omega$ SST turbulence model will be used to obtain pressure snapshots of the flow at periodic intervals. The DMD analysis will be employed on these pressure snapshots. Although either the velocity magnitude snapshots or velocity component snapshots were used in previous studies [12, 13], the pressure flowfield can identify the formation of the dynamic stall vortex (DSV) more easily than the velocity flowfield. Thus, the formation of the DSV and the flow characteristics associated with the DSV can be attributed to the various DMD modes. This is expected to provide physical relevance to the DMD mode shapes. The cycle-to-cycle variations in the airfoil responses will also be investigated with DMD analysis to understand the impact of the stochastic turbulent behavior during dynamic stall.

2 TEST CASE

The light dynamic stall case studied is that of a NACA 0012 airfoil with pitching oscillations about the quarter-chord point. The flow has a Mach number $M_\infty = 0.3$ and Reynolds number $Re_\infty = 4 \times 10^6$. The pitching motion has a reduced frequency of $\bar{f} = 0.1$ and an amplitude of $\alpha_1 = 5^\circ$. The mean angle of attack is $\alpha_0 = 11^\circ$. The unsteady pitching angle of the airfoil can be written as,

$$\alpha(t) = \alpha_0 + \alpha_1 sin(\omega\, t) \tag{1}$$

Equation 1 can be written in terms of nondimensional parameters as,

$$\alpha(t_{nd}) = \alpha_0 + \alpha_1\, sin(2\bar{f} M_\infty\, t_{nd}) \tag{2}$$

The experimental results were presented in [15], which considers a mean angle of attack of 10°. However, the mean angle of attack has been increased here to account for the wall effects analogous to a previous simulation of the present case [16].

3 COMPUTATIONAL SETUP

DDES [17, 18] is performed here using the $k-\omega$ SST turbulence model in EZNSS [19], an in-house code developed by the Israeli CFD center. The unified hybrid RANS/LES DDES in EZNSS is formulated according to Ref. [18]. The mesh used here is an O-type mesh with periodic boundary conditions and consisting of 6.3 million grid points. The mesh dimension is $611 \times 251 \times 41$ with 0.25 chord along the spanwise or Y direction. Grid points are concentrated near the airfoil in order to capture the DSV formation and initial convection. An illustration of the mesh with various levels of magnification is provided in Fig. 1.

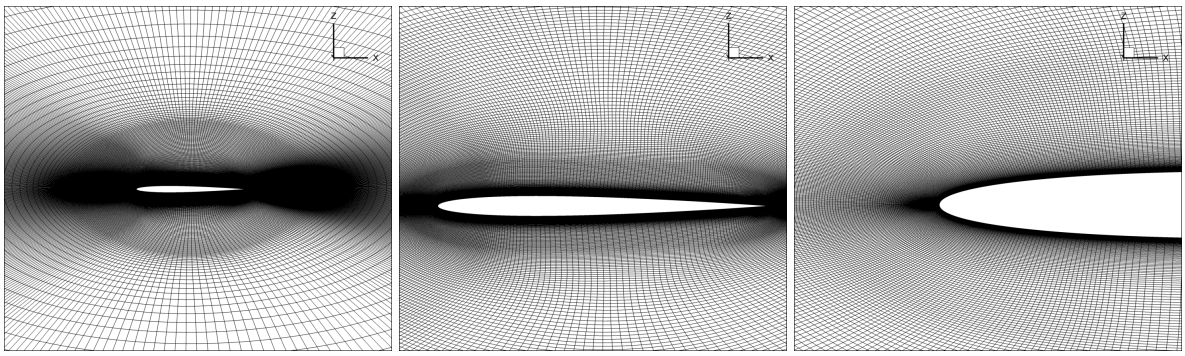

(a) Magnification=50 (b) Magnification=150 (c) Magnification=500

Figure 1: Mesh used for $k-\omega$ SST DDES

Similar to Refs. [12, 13], a reduced computational domain was used for taking the snapshots of the flow. This reduced domain, shown in Fig. 2, consists of a slice around the suction surface of the airfoil including the leading and trailing edges, where most of the phenomena of interest are present. The 3D high-fidelity snapshots generated from the DDES were averaged in the spanwise direction, along the Y direction. The snapshots were sampled in intervals of 17 time steps, where each nondimensional time step for the DDES is 2.053×10^{-2}. Thus, the nondimensional sampling time interval, Δt_{nd}, for obtaining the DMD snapshots is 0.3491,

resulting in 300 snapshots in a single pitch cycle. As explained in Ref. [13], such a sampling rate will not be able to capture the small-scale highly fluctuating structures in the shear-layer but will capture the primary structures of interest. The DDES pitching simulations were carried out with the second-order accurate, dual-time stepping scheme available in EZNSS. The criterion for convergence of the dual-time step solution at each time step is the reduction of the residual by two orders of magnitude (OOM), for both the mean-flow equations and the turbulence model. The criterion for OOM reduction of the residual and the dual-time step procedure in EZNSS has been explained further in Ref. [20].

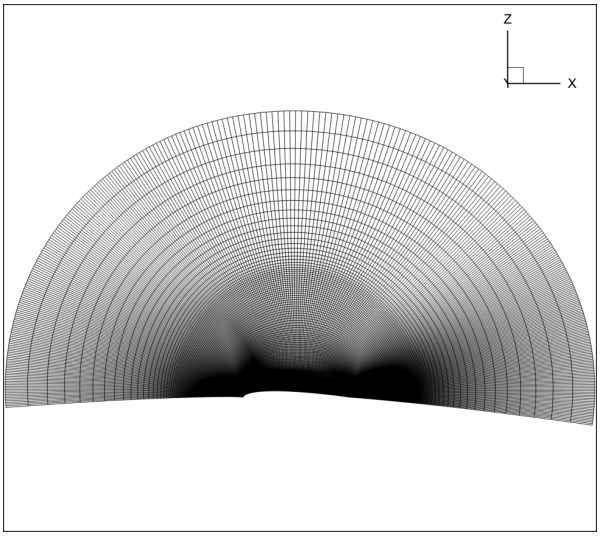

Figure 2: Reduced computational domain used for DMD analysis

4 DYNAMIC MODE DECOMPOSITION

The DMD algorithm used in this article requires snapshots of the flow past the airfoil. The sampling frequency of the snapshots and the pre-processing of the DDES results is discussed in the next section. These snapshots $\boldsymbol{v_i}$ can be arranged as $\boldsymbol{V_1^N}$, $\boldsymbol{V_1^{N-1}}$ and $\boldsymbol{V_2^N}$ as follows:

$$\begin{aligned} \boldsymbol{V_1^N} &= \{\boldsymbol{v_1}, \boldsymbol{v_2}, \ldots, \boldsymbol{v_N}\} \\ \boldsymbol{V_1^{N-1}} &= \{\boldsymbol{v_1}, \boldsymbol{v_2}, \ldots, \boldsymbol{v_{N-1}}\} \\ \boldsymbol{V_2^N} &= \{\boldsymbol{v_2}, \boldsymbol{v_3}, \ldots, \boldsymbol{v_N}\} \end{aligned} \tag{3}$$

where $\boldsymbol{V_1^N} \in \mathbb{R}^{m \times N}$, $\boldsymbol{V_1^{N-1}} \in \mathbb{R}^{m \times N-1}$, $\boldsymbol{V_2^N} \in \mathbb{R}^{m \times N-1}$, $m \gg N$. Here m is the total number of states in the computational domain and N is the number of snapshots. The DMD assumes a linear mapping $\boldsymbol{A}$ to approximate the nonlinear dynamical system. This mapping governs the evolution of the system from one time instant to the next time instant. Thus,

$$\boldsymbol{v_{i+1}} = \boldsymbol{A v_i} \tag{4}$$

The linear system can be represented as

$$\boldsymbol{A V_1^{N-1}} = \boldsymbol{V_2^N} \tag{5}$$

Employing a Krylov sequence in terms of $\boldsymbol{A}$ and $\boldsymbol{v_1}$,

$$\boldsymbol{V_1^N} = \left\{\boldsymbol{v_1}, \boldsymbol{A v_1}, \boldsymbol{A}^2\boldsymbol{v_1}, \ldots, \boldsymbol{A}^{N-1}\boldsymbol{v_1}\right\} \tag{6}$$

the final snapshot can be written as a linear combination of the preceding snapshots.This assumption is made for a sufficiently large of numbers of snapshots when the vectors become linearly independent

$$\boldsymbol{v_N} = a_1\boldsymbol{v_1} + a_2\boldsymbol{v_2} + \ldots + a_{N-1}\boldsymbol{v_{N-1}} + \boldsymbol{r} \tag{7}$$

where $\boldsymbol{r}$ denotes the residual. Considering $\boldsymbol{a}^T = \{a_1, a_2, \ldots, a_{N-1}\}$,

$$\boldsymbol{v_N} = \boldsymbol{V_1^{N-1}}\boldsymbol{a} + \boldsymbol{r} \tag{8}$$

Since there is no *a priori* knowledge of $\boldsymbol{A}$, an approximation is required. Thus, a companion matrix $\boldsymbol{S}$ is built as the approximation to $\boldsymbol{A}$ by expressing the final snapshot as a linear combination of the previous snapshots.

$$\boldsymbol{A}\left\{\boldsymbol{v_1}, \boldsymbol{v_2}, \ldots, \boldsymbol{v_{N-1}}\right\} = \left\{\boldsymbol{v_2}, \boldsymbol{v_3}, \ldots, \boldsymbol{v_N}\right\} \tag{9}$$

$$\implies \boldsymbol{A}\left\{\boldsymbol{v_1}, \boldsymbol{v_2}, \ldots, \boldsymbol{v_{N-1}}\right\} = \left\{\boldsymbol{v_2}, \boldsymbol{v_3}, \ldots, \boldsymbol{V_1^{N-1}}\boldsymbol{a}\right\} + \boldsymbol{r}\boldsymbol{e}_{N-1}^T \tag{10}$$

$$\implies \boldsymbol{A}\boldsymbol{V_1^{N-1}} \equiv \boldsymbol{V_1^{N-1}}\boldsymbol{S} + \boldsymbol{r}\boldsymbol{e}_{N-1}^T \tag{11}$$

$$\implies \boldsymbol{V_2^N} \equiv \boldsymbol{V_1^{N-1}}\boldsymbol{S} + \boldsymbol{r}\boldsymbol{e}_{N-1}^T \tag{12}$$

with $\boldsymbol{e}_{N-1} \in \mathbb{R}^{N-1}$ as $(N-1)$th unit vector. The companion matrix $\boldsymbol{S}$ is of the form,

$$S = \begin{bmatrix} 0 & & & & & a_1 \\ 1 & 0 & & & & a_2 \\ & \ddots & \ddots & & & \vdots \\ & & & 1 & 0 & a_{N-2} \\ & & & & 1 & a_{N-1} \end{bmatrix} \tag{13}$$

To be able to compute the $\boldsymbol{S}$ matrix, a Singular Value Decomposition (SVD) of $\boldsymbol{V_1^{N-1}}$ is performed,

$$SVD\left(\boldsymbol{V_1^{N-1}}\right) = \boldsymbol{U}\boldsymbol{\Sigma}\boldsymbol{W}^H \tag{14}$$

where $\boldsymbol{W}^H$ is the conjugate transpose of $\boldsymbol{W}$, $\boldsymbol{U} \in \mathbb{C}^{m\times N-1}$, $\boldsymbol{W} \in \mathbb{C}^{m\times N-1}$, $\boldsymbol{\Sigma} \in \mathbb{C}^{N\times N}$. Thus,

$$\boldsymbol{V_2^N} = \boldsymbol{U}\boldsymbol{\Sigma}\boldsymbol{W}^H\boldsymbol{S} \tag{15}$$

Finally, the matrix $\tilde{\boldsymbol{S}}$ can be obtained by projecting $\boldsymbol{A}$ on the subspace of $\boldsymbol{U}$.

$$\tilde{\boldsymbol{S}} = \boldsymbol{U}^H\boldsymbol{V}_2^H\boldsymbol{W}\boldsymbol{\Sigma}^+ \in \mathbb{C}^{N-1\times N-1} \tag{16}$$

where $\boldsymbol{\Sigma}^+$ is the pseudo-inverse of $\boldsymbol{\Sigma}$, $\boldsymbol{\Sigma}^+ = \left(\boldsymbol{\Sigma}^H\boldsymbol{\Sigma}\right)^{-1}\boldsymbol{\Sigma}^H$. $\tilde{\boldsymbol{S}}$ is the desired approximation of $\boldsymbol{A}$ obtained by projecting $\boldsymbol{A}$ on the subspace of $\boldsymbol{U}$. The DMD modes are finally computed with an eigenvalue decomposition of the $\tilde{\boldsymbol{S}}$ matrix, resulting in the eigenvectors $\boldsymbol{y}_i$ and eigenvalues μ_i such that

$$\tilde{\boldsymbol{S}}\boldsymbol{y}i = \mu_i\boldsymbol{y}i \tag{17}$$

The DMD modes are then obtained as

$$\phi_i = \boldsymbol{U}\boldsymbol{y}_i \tag{18}$$

where $\boldsymbol{U}$ is the right singular vector of $\boldsymbol{V_1^{N-1}}$ and $\boldsymbol{y}_i$ are the eigenvectors of $\tilde{\boldsymbol{S}}$. The approximate eigenvalues λ obtained from the DMD are expressed by

$$\lambda = \frac{log\,(\mu)}{\Delta t} \tag{19}$$

where Δt is the time interval between subsequent snapshots. These eigenvalues can be used to study the stability characteristics of the modes. Positive $\Re\,(\lambda)$ and negative $\Re\,(\lambda)$ denote unstable and stable modes, respectively. A neutrally stable mode has a zero real part. $\Im\,(\lambda)$ provides the damped frequency of each DMD mode. The mean flow is a special case having a zero eigenvalue, thus showing it is time-invariant. The eigenvalues obtained are usually complex conjugate pairs having the same stability characteristics but different signs. Neglecting negative frequencies, each conjugate mode pair represent a single DMD mode.

Reconstruction

The DMD can be written as follows,

$$\boldsymbol{v}_i = \sum_{k=1}^{N} \alpha_k (\mu_k)^{i-1} \boldsymbol{\phi}_k \tag{20}$$

The DMD modes can be used for reconstruction of the flow by using equation 20. For $k = 1$, α_k can be obtained from eq. 20 as,

$$\boldsymbol{v}_1 = \sum_{k=1}^{l} \alpha_k \boldsymbol{\phi}_k = \boldsymbol{\phi_r}\boldsymbol{\alpha} = \boldsymbol{U}\boldsymbol{y_r}\boldsymbol{\alpha}$$

$$\Rightarrow \boldsymbol{\alpha} = \boldsymbol{Y_r}^{-1}\boldsymbol{U}^H\boldsymbol{v}_1 \tag{21}$$

where $Y_r = [y_1\ y_2\ ...y_l] \in \mathbb{C}^{m\times l}$. α can be substituted in eq. 20 to obtain the reconstructed solution.

5 RESULTS

5.1 DDES results

Four cycles of DDES of the pitching airfoil is performed in EZNSS. The phase-averaged lift coefficient, cl, and the pitching moment at the quarter-chord, $cm_{y,x/c=0.25}$ are obtained from the corresponding responses of the four cycles of DDES. The phase-averaged results are compared against available experimental results in Fig. 3. Overall, the phase-averaged DDES results show a close correlation to the experimental results. However, there are some differences between the experimental results and the DDES predictions during the pitch-down phase. The largest differences are observed just after the moment and lift stall, when the flow slowly recovers

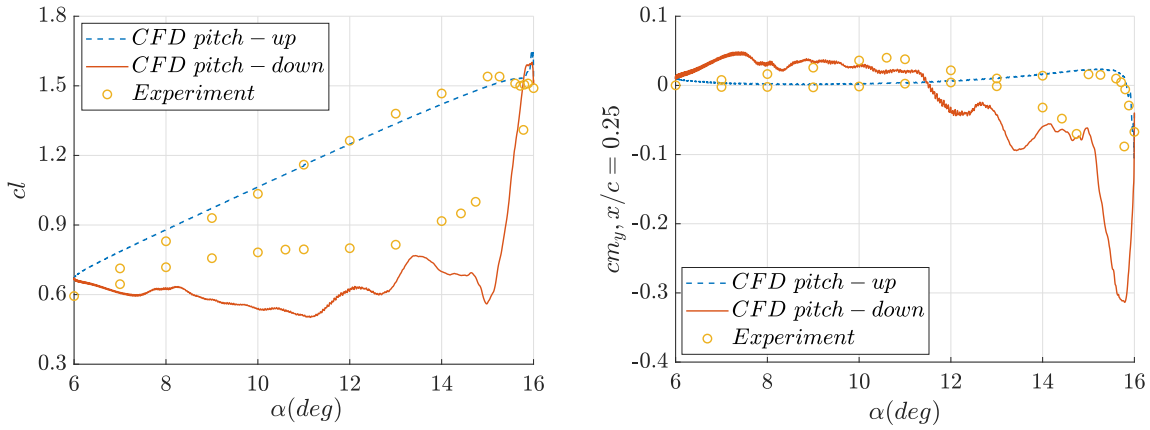

(a) Lift coefficient (b) Pitching moment at quarter chord

Figure 3: Comparison of $k-\omega$ SST DDES results with experiments

from the stall. Similar behavior has been observed and explained in other dynamic stall studies [21–23].

The phase-averaged pitching moment coefficient at the quarter-chord is compared to the pitching moment coefficients for cycle 1 and cycle 3 of the DDES in Fig. 4. Significant fluctuations between the pitching moment coefficients are observed during the downstroke, especially during the recovery from stall phase. As explained in a recent review article on dynamic stall [23], the recovery from stall is somewhat of a stochastic process and significant differences in the aerodynamic loads between subsequent pitching cycles are expected. A cycle-averaged aerodynamic damping coefficient, Ξ_{cycle}, is also presented in Fig. 4 for the three cases. Ξ_{cycle} is defined in Ref. [23] as follows:

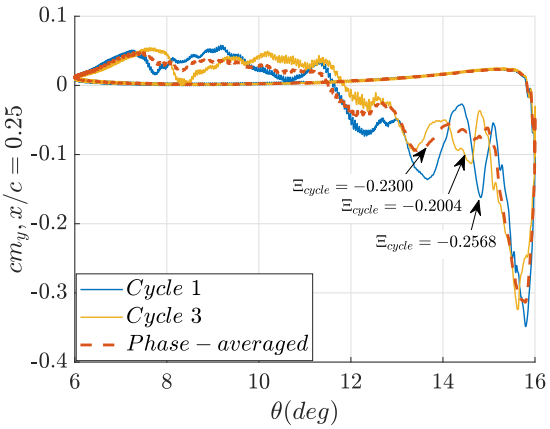

Figure 4: Cycle-to-cycle variations in pitching moment at quarter-chord and aerodynamic damping

$$\Xi_{cycle} = -\frac{1}{\pi {\alpha_1}^2} \oint cm_{y,x/c=0.25} d\alpha \tag{22}$$

The cycle aerodynamic damping can also be computed from the area enclosed in the cycle variation of the pitching moment coefficient as:

$$\Xi_{cycle} = \frac{1}{\pi {\alpha_1}^2} \int_{\alpha_{min}}^{\alpha_{max}} \left({cm_{y,x/c=0.25}}^D - {cm_{y,x/c=0.25}}^U \right) d\alpha \tag{23}$$

where superscripts U and D denote the pitch-up and pitch-down phase of the airfoil motion. The pitching moment coefficient is generally computed at the pitching axis, which for our case is the quarter-chord. Thus, when energy is transferred from the airstream to the airfoil, the aerodynamic damping is negative indicating that the dynamic system is unstable. Such a dynamic stall phenomenon can drive an aeroelastic system towards stall flutter. The cycle-averaged aerodynamic damping for the three cases presented in Fig. 4 is negative, indicating the potential of stall-induced instability, like stall flutter, for an elastic system attached to the present aerodynamic system. The Ξ_{cycle} for the experimental case is -0.05, which is also negative. It is also important to note that although all the three cases presented in Fig. 4 show negative Ξ_{cycle}, their values are somewhat different from one another due to the cycle-to-cycle fluctuations.

The present comparison between the experimental and DDES results is quite different than that provided in a similar simulation [16]. It was observed that the results obtained in Ref. [16] with a very coarse mesh are mesh dependent. Also, only a single cycle was presented in Ref. [16], thus neglecting the cycle-to-cycle variations during recovery from stall.

The dynamic stall phenomena is further investigated by looking at the negative pressure coefficient, $-cp$, on the upper surface of the airfoil at different phases of the pitching motion Φ, and comparing it to the cl and $cm_{y,x/c=0.25}$ variations with the phase in Fig. 5. Here, we define the phase as $\Phi = \omega t$. Fig. 5 (a) shows a large suction at the leading edge of the airfoil till $\Phi = 80^\circ$ ($\alpha = 14.2^\circ$). This is denoted as the leading edge suction (LE suction) phase of the dynamic stall. At $\Phi = 80^\circ$ ($\alpha = 14.2^\circ$), a locally formed high suction region is observed at about 35% of the chord, indicating the formation of the dynamic stall vortex (DSV). As expected for the light dynamic stall regime at high Reynolds number, the DSV is formed at the location of maximum airfoil thickness. Such a behavior was reported earlier and explained in Refs. [2, 15]. We can also observe that the DSV formed at $\Phi = 80^\circ$ ($\alpha = 14.2^\circ$), eventually moves along the airfoil and leaves the trailing edge at $\Phi = 125^\circ$ ($\alpha = 15.44^\circ$). Another locally formed high suction region at the trailing edge at $\Phi = 125^\circ$ ($\alpha = 15.44^\circ$) is considered the trailing edge vortex (TEV). The moment stall is observed around $\Phi = 85^\circ$ ($\alpha = 14.38^\circ$), shortly after the formation of the DSV. The pitching moment coefficient at the quarter chord decreases as the DSV travels towards the trailing edge of the airfoil. The lift stall is observed around $\Phi = 105^\circ$ ($\alpha = 14.97^\circ$) as the DSV reaches the trailing edge. While the airfoil recovers from the moment stall, the cl reduces further as the DSV leaves the trailing edge completely. Eventually, the flow reattaches and the airfoil recovers from both the lift and moment stall.

Four snapshots of the suction ($-cp$) flowfield are shown in Figures 6 (a)-(d), at $\Phi = 60^\circ$, 81.6°, 108.8° and 122.4°, respectively. At $\Phi = 60^\circ$ we don't see the DSV yet but the LE suction can be observed. At $\Phi = 81.6^\circ$, we see the formation of the DSV at $x/c = 0.35$. The DSV increases in strength, travels towards the trailing edge (6 (c)) and eventually leaves the trailing edge (Figure 6 (d)) at $\Phi = 122.4^\circ$ in the form of the TEV. The DMD analysis will be performed on the pressure snapshots to investigate the modal participation in the dynamic stall phenomena explained here.

The upper surface suction for the four cycles of DDES is illustrated in Fig. 7 (a)-(d) to investigate the cycle-to-cycle variations in the aerodynamic loading observed in Fig. 4. We can see

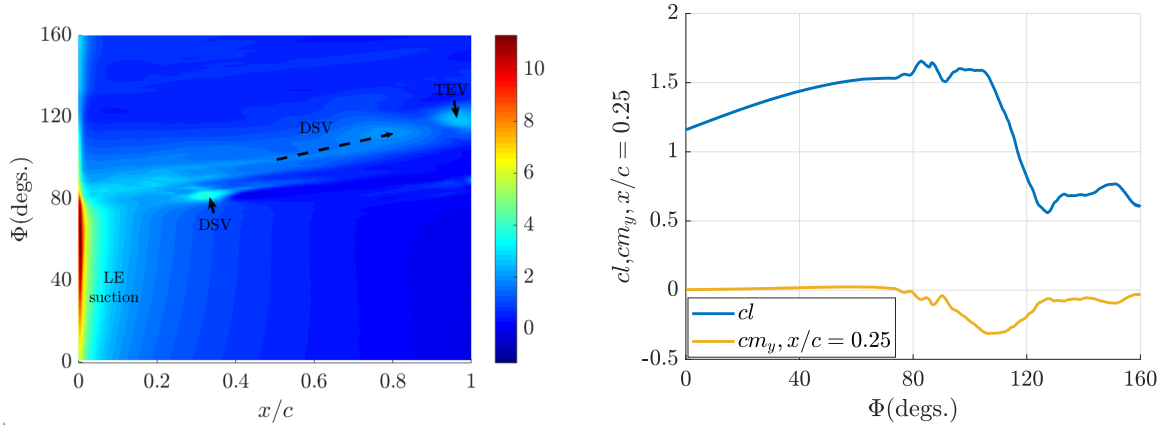

(a) Upper surface -*cp* (b) cl and $cm_{y,x/c=0.25}$

Figure 5: Variation of aerodynamic forces with change in the phase of the pitching motion

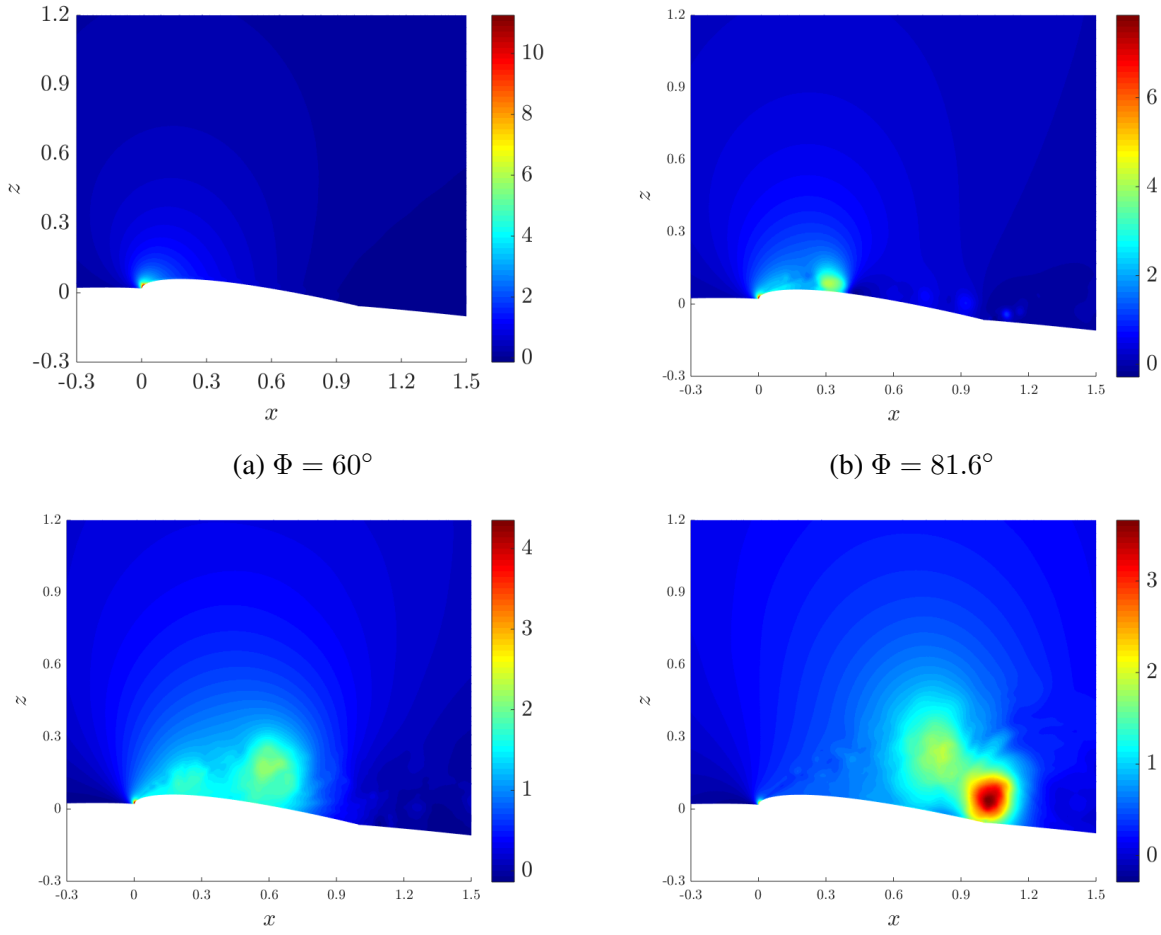

(a) $\Phi = 60°$ (b) $\Phi = 81.6°$

(c) $\Phi = 108.8°$ (d) $\Phi = 122.4°$

Figure 6: Snapshots of -*cp* at various phases of pitching

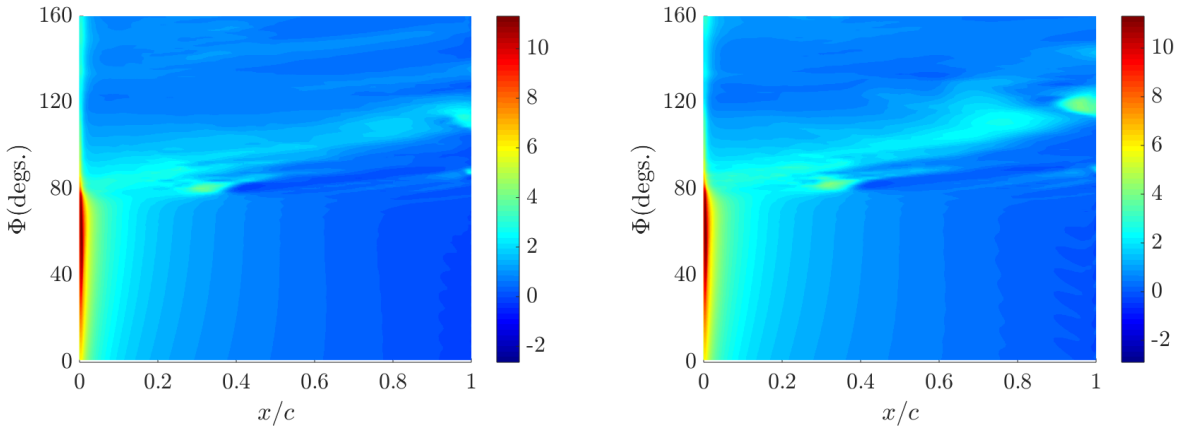

(c) Cycle 1

(d) Cycle 2

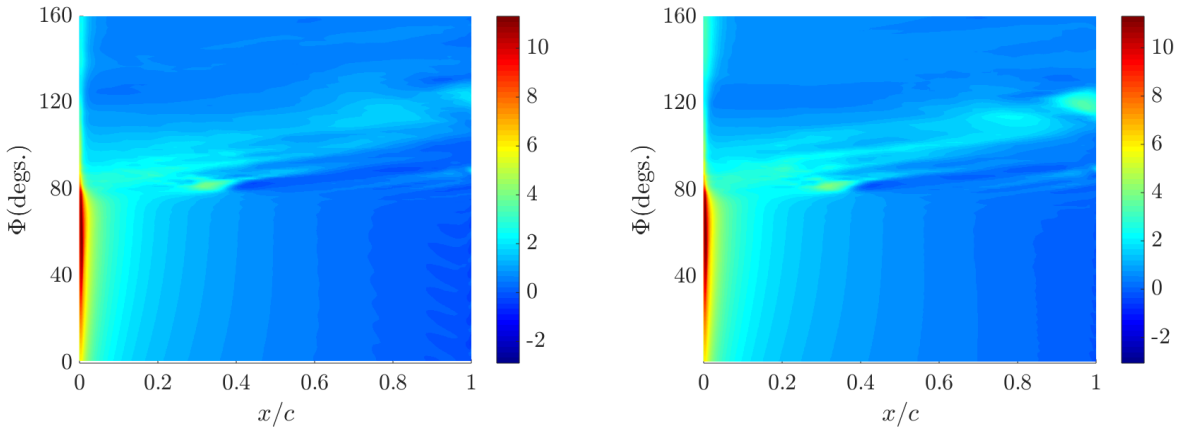

(c) Cycle 3

(d) Cycle 4

Figure 7: Cycle-to-cycle variations in upper surface suction coefficient, $-cp$

that in the four cases, the location of the DSV formation remains fixed at 35% of the chord. However, the strength of the leading edge suction and extent of the suction from the leading edge varies from cycle to cycle. The suction contours representing the strength of the DSV traveling towards the trailing edge and the strength of the TEV also vary from cycle to cycle. The strength of the vortices is significantly larger for cycles 2 and 4 (7 (b), (d)). The strength of the TEV is minimum for cycle 3 (7 (c)). The phase of the various features shown here also varies slightly from cycle to cycle. Thus, the phase-averaging acts as a smoothing process and the levels of the contours of the phase-averaged upper surface suction, shown in fig. 5 (a), are slightly different than those observed here. The cycle aerodynamic damping calculated via equation 23 has a minimum value for cycle 1 (-0.2568) and maximum value for cycle 3 (-0.2004). Cycles 2 and 4 have intermediate values (-0.2331 and -0.2316, respectively) of cycle aerodynamic damping. The pressure snapshots of these four cycles will also be analyzed with DMD to investigate the pressure modes, which lead to such varying behavior of the DSV and also the varying cycle-averaged aerodynamic damping.

5.2 DMD analysis

5.2.1 Phase-averaged pressure snapshots

The DMD analysis was performed on the phase-averaged snapshots of the pressure coefficient cp. In earlier DMD analysis of dynamic stall phenomena, either the snapshots of the stream-

wise velocity component [13], or the velocity magnitude [12] was used for computing the DMD modes. However, the pressure coefficient provides a clearer indication of the leading edge suction, the formation of the DSV, its movement along the airfoil and the TEV, than the velocity flowfield. Thus, the DMD pressure modes are used to investigate these important features of the dynamic stall phenomenon.

As explained earlier, the DMD modes obtained from the analysis have complex conjugate pairs of eigenvalues except for the first mode, which has a real eigenvalue. Each mode pair having complex conjugate eigenvalues will be denoted a single DMD mode number. All the DMD modes, except the first mode, have frequencies that are multiples of the pitching motion frequency. They were ranked in ascending order of their modal amplitude. Figure 8 (a) shows the reduced frequencies of the various modes, normalized by the reduced frequency of the pitching motion. We can see from the scattered nature of the reduced frequency plot that when the modes are ranked according to their modal amplitude, except for modes 2-5, the subsequent modes are not the higher harmonics of the pitching motion frequency. This indicates that the higher modes may have a higher contribution to the pressure flow field than some of the lower modes. The variation of the modal amplitude is shown in Fig. 8 (b). We can see that the modal amplitude of the first 5 modes is much higher than the rest of the modes. The amplitude of mode 5 is over an order of magnitude lower than that of mode two. However, the relatively flat nature of the modal amplitude curve from mode 6 onward shows that the modal contribution to the dynamic stall phenomena is non-negligible.

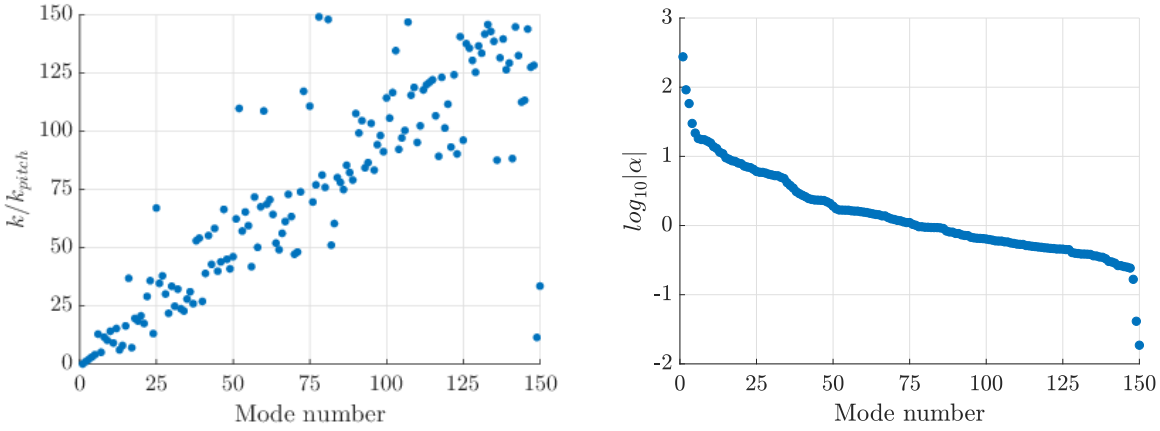

(a) Normalized reduced frequency, k/k_{pitch}

(b) Modal amplitude

Figure 8: DMD modes ranked according to $|\alpha|$

The first seven DMD modes are presented in Table 1 along with their eigenvalues and reduced frequencies. The table shows that the first mode, having a zero eigenvalue, is a stationary mode. This mode represents the mean flow and should also be obtained by time-averaging the phase-averaged pressure snapshots. This is demonstrated in Fig. 9, where the 1st DMD mode, multiplied with its modal amplitude, has been compared to the time-averaged mean pressure flowfield obtained from the DDES. The two cases have a very similar flowfield and also the same magnitude of the suction contours. This can be further concluded by looking at the differences in the $-cp$ between DMD mode 1 and the time-averaged DDES solution in Fig. 10, which shows that the differences are more than two orders of magnitude smaller than the actual cp values. Looking at mode 2 from Table 1, we observe that this mode has the same reduced frequency of 0.1 as that of the pitching excitation provided to the airfoil. The next

Table 1: Eigenvalues and reduced frequency of DMD modes

Mode	Eigenvalue (μ_k)	Reduced frequency ($\bar{f}$)
1	1.0	–
2	$0.9997 \pm 0.0209i$	0.1000
3	$0.9992 \pm 0.0420i$	0.2007
4	$0.9983 \pm 0.0626i$	0.2990
5	$0.9961 \pm 0.0832i$	0.3977
6	$0.9570 \pm 0.2634i$	1.2822
7	$0.9936 \pm 0.1049i$	0.5022

higher modes 3-5 can be considered the higher harmonics of the pitching motion. Mode 6 has a frequency that is thirteen times the pitching frequency, but is ranked ahead of the fourth harmonic, mode 7, because of its higher modal amplitude.

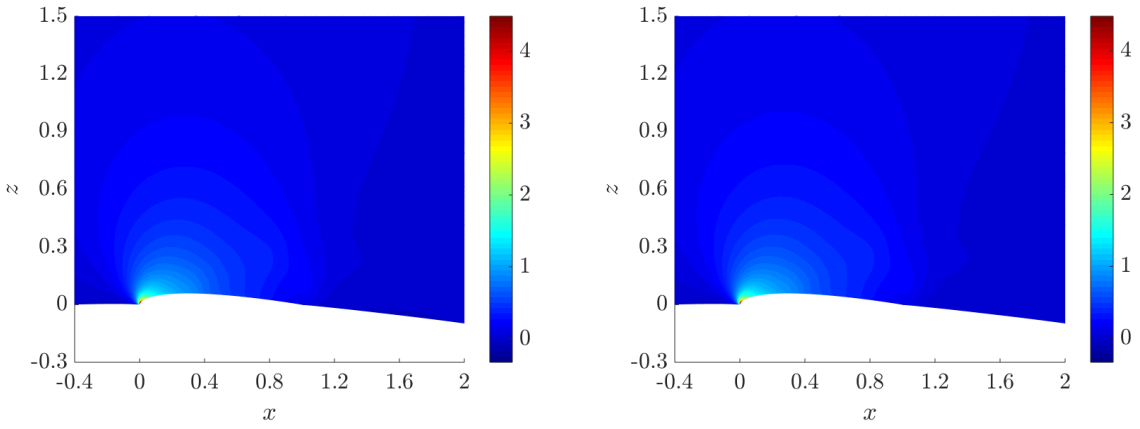

(a) Time-averaged DDES pressure snapshots

(b) DMD mode 1

Figure 9: Comparison of $-cp$

Next, each the complex conjugate pairs associated with each of the modes 2-7, were multiplied with their corresponding complex conjugate modal amplitudes via equation 20, to obtain real-valued cp values. Here, $N = 2$ in equation 20 as we are applying the equation on the complex conjugate pair of a DMD mode. The variation of the surface suction distribution of MD modes 2-7, with the phase of the pitching motion, is presented in Figures 11 (a)-(f). It can be seen that although mode 2 has a large relative modal amplitude compared to the higher modes, the formation of DSV is not clearly evident from it. Only a LE suction region can be distinctly identified in this mode, which has the same phase as that of the traveling DSV in the surface pressure plot in figure 5 (a). Modes 3 and 4 are the subsequent higher harmonics of mode 2. The formation of the DSV can be identified in mode 4 based on the concentrated suctions at 35% of the chord. However, the high suction values along the chord indicate the travel of the DSV in all the modes 2-4.

Modes 5, 6 and 7 show the formation of the DSV at 35% of the chord and its eventual movement towards the trailing edge much more clearly. Mode 6 also clearly shows the TEV which is not clearly evident in the other DMD modes shown here. Modes 5, 6 and 7 also show significant

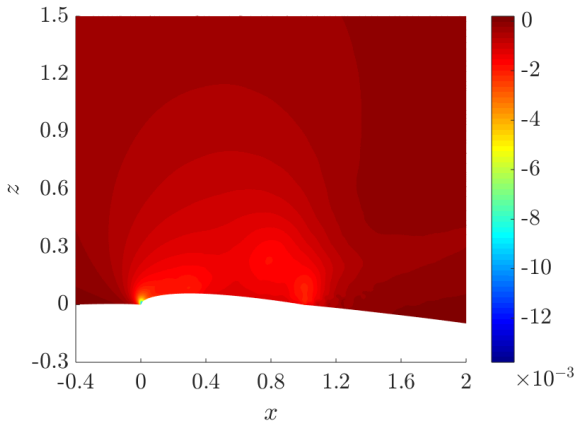

Figure 10: Defference between the $-cp$ obtained from time-averaged DDES pressure snapshots and DMD mode 1

damping and decay of the modal features with an increase in the period number. The features observed in modes 5, 6 and 7 closely resemble that of the surface pressure distribution in fig. 5 (a), although the energy content in these modes is relatively much lower than modes 2, 3 and 4. This indicates that for the light dynamic stall phenomena at the high, turbulent Reynolds number presented here, higher modes with relatively lower modal participation show important physical phenomena that are sometimes not observed in the larger energy modes. This is especially true for the formation of the DSV and its travel towards the trailing edge of the airfoil, as several higher modes show these features much more clearly than the lower modes. This is significantly different from what was concluded in a previous DMD analysis of deep stall of a plunging airfoil at lower Reynolds number [13].

To develop a reduced-order model with the DMD modal ranking presented earlier, the $L2$ error norm between the cp snapshots and the reconstructed solutions were computed as follows:

$$L2\ error(\%) = \left\| \frac{\sqrt{\left[\sum_{i=1}^{G} (\boldsymbol{cp}_{reconstructed} - \boldsymbol{cp}_{DDES})^2\right]}}{\sqrt{\left[\sum_{i=1}^{G} \boldsymbol{cp}_{DDES}{}^2\right]}} \right\| \tag{24}$$

where G represents the total number of grid points in the reduced computational domain used for performing the DMD analysis. These are presented for 5 cases: N =9,19, 29, 49 and 99, in figure 12, where N represents the total number of modes including the complex conjugate pairs. Thus, N =9 represents the stationary mode and four DMD mode pairs. The largest $L2$ error norms are observed during the formation of the DSV phase and its travel towards the trailing edge, from $\phi = 80° - 130°$. Once the DSV leaves the trailing edge and the airfoil recovers from stall, the error between the reconstructed solution and original snapshot decreases. As expected, the $L2$ error norms decreased with increasing the number of modes in the reconstructed solution. With N =99 a peak error of 11% was observed at $\Phi = 86.4°$. The reconstructed upper surface suction distribution along the airfoil with the phase of motion, for $N = 49$ and $N = 99$, are compared to their counterpart obtained from the DDES in figure 13. We can see that for $r = 49$ (fig. 13 (b)) the DSV at 35% of the chord and the TEV are not completely developed compared to the DDES results (13 (a)). However, for $r = 99$ (fig. 13 (c)) much better correlation

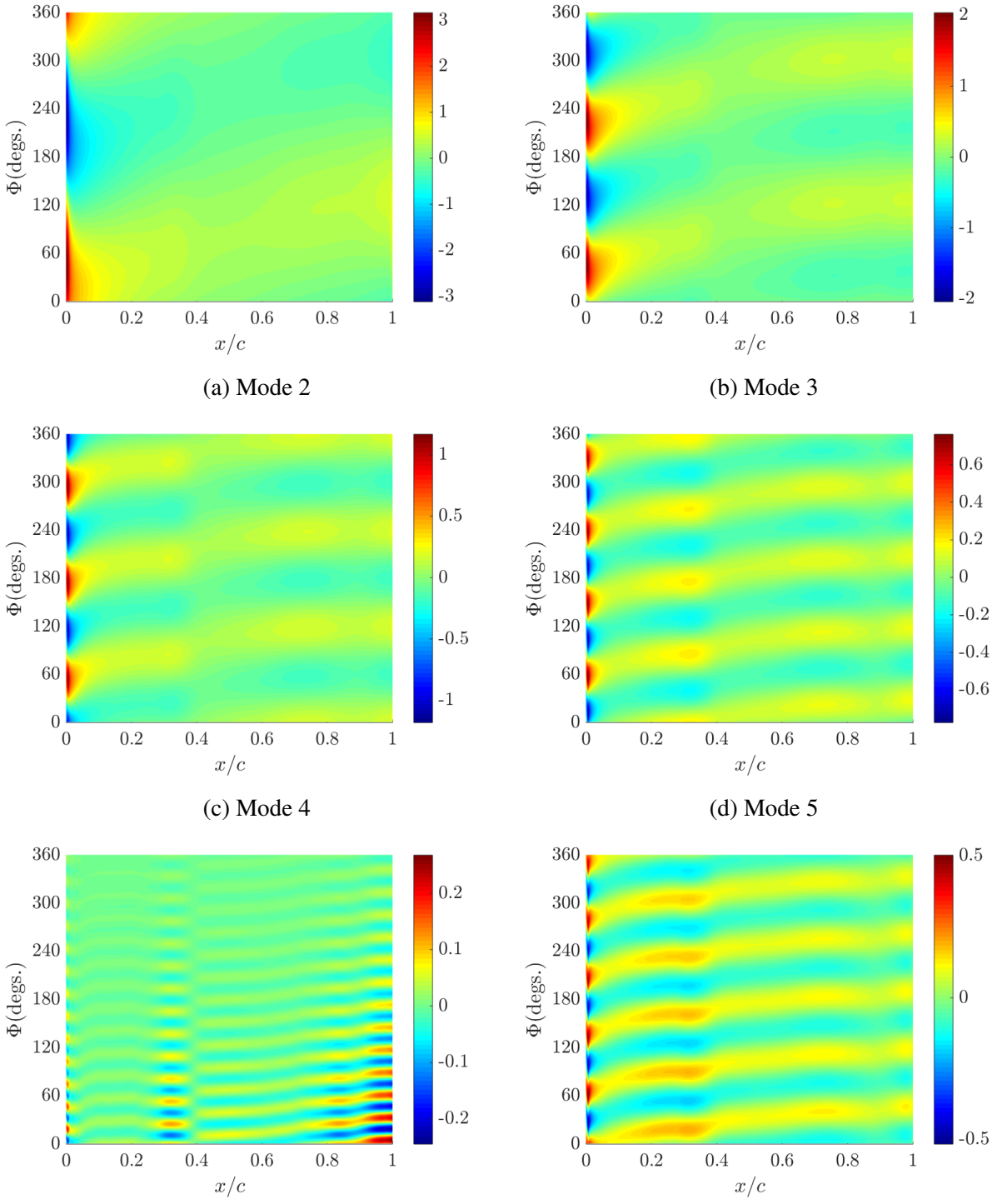

(a) Mode 2

(b) Mode 3

(c) Mode 4

(d) Mode 5

(e) Mode 6

(f) Mode 7

Figure 11: Change in upper surface -*cp* distribution along the airfoil with the phase of the pitching motion for DMD modes 2-7

is observed between the DSV and the TEV of the reconstructed solution compared to their counterparts from the DDES snapshots.

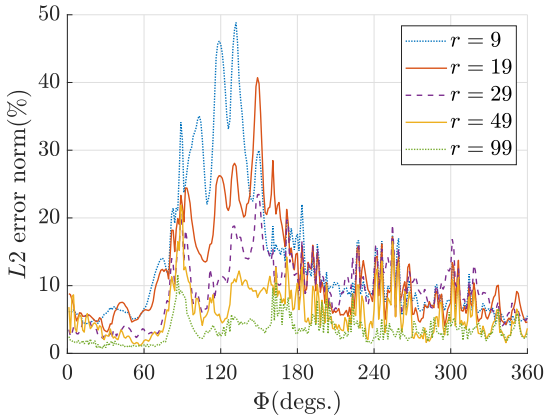

Figure 12: $L2$ error norm between the reconstructed solution and DDES pressure snapshots for various model orders

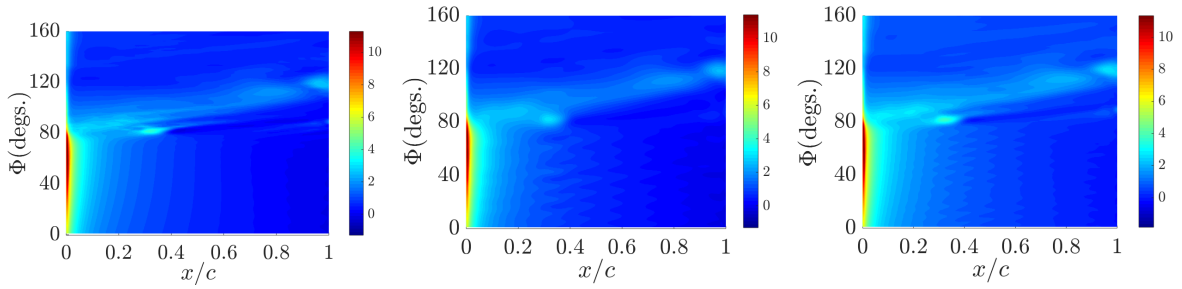

(a) DDES results (b) DMD reconstruction, r=49 (c) DMD reconstruction, r=99

Figure 13: Comparison of upper surface suction, $-cp$

The DMD analysis was also used to investigate the contribution of the various modes to the cycle-averaged aerodynamic damping. Since the DMD analysis was performed on a reduced computational domain consisting mainly consisting of the upper surface of the airfoil, the $cm_{y,x/c=0.25}$ was computed with only the airfoil surface grid points of the reduced computational domain. The $cm_{y,x/c=0.25}$ thus computed for the DDES snapshots are shown in Fig. 14 (a). It can be observed from Fig. 3 (b) that the $cm_{y,x/c=0.25}$ for the reduced computational domain shows reasonable correlation with its counterpart computed for the full domain. The $cm_{y,x/c=0.25}$ was also computed for the various DMD modes and is presented for DMD mode 2 in Fig. 14 (b). These $cm_{y,x/c=0.25}$ values for the full solution and various DMD modes were used for computing the cycle aerodynamic damping via equation. 23. The aerodynamic damping coefficients for the various DMD modes, $\Xi_{cycle,DMD}$, are presented in Table 2. The aerodynamic damping coefficients normalized by the damping coefficient of the DDES solution, $|\Xi_{cycle,DDES}|$, are also presented in Table 2. It can be observed that since DMD mode 1 is a stationary mode, it does not have any aerodynamic damping. DMD mode 2 has a negative aerodynamic damping coefficient thus showing the potentially unstable nature of the mode. Also, a relative damping coefficient of 0.9958 indicates that it contributes almost all of the negative aerodynamic damping of the full solution. The contribution of modes 3-8 to the aerodynamic damping is negligible.

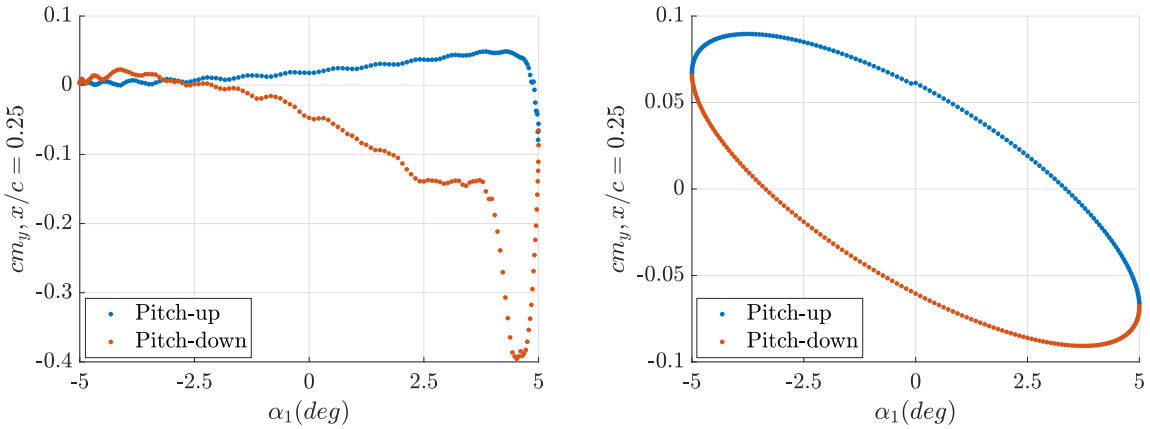

(a) DDES pressure snapshots

(b) DMD pressure mode 2

Figure 14: Comparison of $cm_{y,x/c=0.25}$ obtained for the reduced computational domain computed

Table 2: Normalized cycle aerodynamic damping of various DMD modes

DMD Mode	$\Xi_{cycle,DMD}$	$\Xi_{cycle,DMD}/\Xi_{cycle,DDES}$
1	0	0
2	-0.7003	0.9958
3	-2.1e-04	3.1e-04
4	-0.0043	0.0061
5	0.0037	-0.0053
6	9.3e-04	-0.0013
7	-0.0036	0.0052
8	-0.0045	0.0078

From figure 14 (b), it can be observed that the $cm_{y,x/c=0.25}$ of DMD Mode 2 has a phase lead of a little over $90°$ to the pitching oscillation. This phase lead generates positive work thus creating the negative aerodynamic damping coefficient. We can conclude that the DMD mode having the frequency of the prescribed motion, and primarily showing the LEV and the path of the DSV's travel along the airfoil, contributes the most to the negative cycle-averaged aerodynamic damping of light dynamic stall phenomena at high, turbulent Reynolds number.

5.2.2 Cycle-to-cycle variations

Next, DMD analysis is performed to obtain the pressure modes for various cycles of the pitching oscillation. The differences in the pressure modes and the eigenvalues associated with them will be investigated to understand the role of the DMD modes in the cycle-to-cycle variations often observed in the aerodynamic responses during dynamic stall. It was observed that with the present number of DDES snapshots captured in each cycle, the DMD analysis did not converge if the snapshots from only one cycle are considered. Such non-convergence of DMD can be expected when a sufficient number of observables or snapshots are not used for generating the DMD modes. Thus, the total number of snapshots from two cycles were phase-averaged and then used for the DMD analysis to obtain converged results. The two cases presented here are phase-averaged results from cycles 1 and 2, and cycles 2 and 3. The first case, which is denoted as *PA cycle 1-2*, has a phase-averaged cycle aerodynamic damping of -0.2810. The second case, denoted as *PA cycle 2-3*, has a phase-averaged cycle aerodynamic damping of -0.2164. The phase-averaged results obtained from four cycles is denoted as *PA cycle 1-4*. It has a cycle aerodynamic damping of -0.2300 lying in between the corresponding values of the other two cases. *PA cycle 1-2* and *PA cycle 2-3* will be analyzed further with the help of the DMD modes and compared to the already obtained *PA cycle 1-4* results.

The modal displacements of the DMD modes are sorted based on their amplitude for the three cases mentioned earlier and presented in figure 15. It is observed that for modes 1-3 the modal amplitude for the three cases is similar. For mode 4, *PA cycle 1-2* has a slightly lower modal amplitude than the other two cases. From mode 5 onward, somewhat different modal amplitudes are observed for the three cases. Overall, the three cases show a similar pattern of modal amplitude and modes 1-4 comprises most of the energy of the flow.

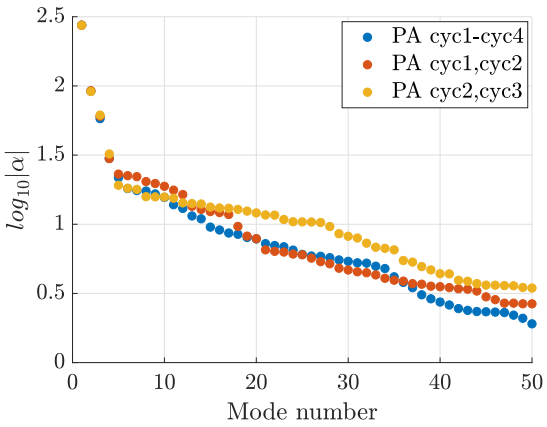

Figure 15: Comparison of modal displacements (ranked according to $|\alpha|$) between DMD analysis of various phase-averaged pressure snapshots

The reduced frequency spectrum of three cases for the first 50 modes, sorted according to their

modal amplitude, are presented in figure 16. Figure 16 is the same as fig. 8 (a), but only showing the first 50 modes. The reduced frequency spectrum for all the three cases is highly scattered indicating that for all the three cases, the higher frequency modes often have a larger modal amplitude than their lower frequency counterparts. Hence, they are expected to provide a significant contribution to the physical phenomena observed here. Mode 1 is the stationary mode for all three cases. Modes 2 and 3-4 are the modes with the frequency of pitching and its higher harmonics, respectively, for all the three cases. The mode 5 for *PA cycle 1-2* is not the third harmonic, unlike the other two cases. Similarly, mode 6 for *PA cycle 3-4*, is a much higher harmonic with a much larger frequency than its counterparts for the other two cases. This shows the significantly different cycle-to-cycle modal participation observed during dynamic stall. Such different pressure modes lead to tangible differences in the cycle to cycle surface pressure distribution, as observed in fig. 7.

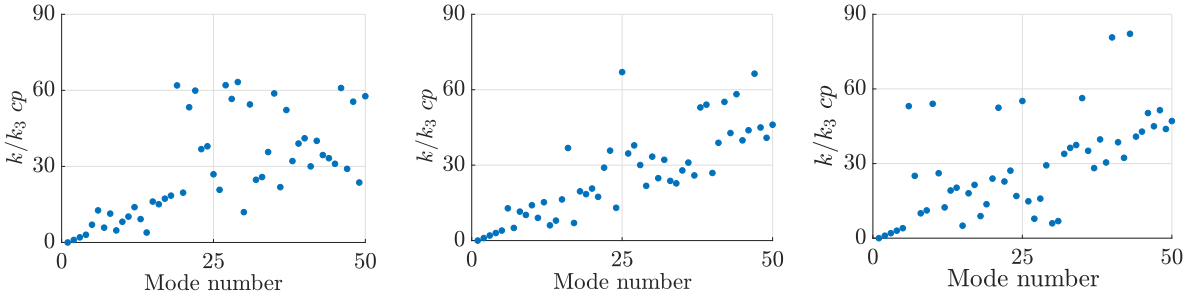

(a) Phase-averaged cycle 1-2 (b) Phase-averaged cycle 1-4 (c) Phase-averaged cycle 2-3

Figure 16: Comparison of modal reduced frequency (ranked according to $|\alpha|$) between DMD analysis of pressure snapshots

DMD modes 3, 4, 5 and 6 from the three cases are compared in figures 17, 18, 19 and 20. From figures 17 and 18, we see that modes 3 and 4 are the first and second harmonic modes, respectively, for all the cases. However, from 18 (a) it is not evident that mode 4 for *PA cycle 1-2* is unstable and has a positive real part of the eigenvalue. Mode 3 does not clearly show the DSV formation which can be clearly observed in mode 4. From fig. 19 (a) it is observed that mode 5 for *PA cycle 1-2* is a higher harmonic than its counterparts. Also, it can be observed that in mode 5 for *PA cycle 2-3* the DSV at 35% of the chords grows from one period to another. Mode 6 of *PA cycle 2-3* in fig. 20 (c) is a much higher harmonic than its counterparts.

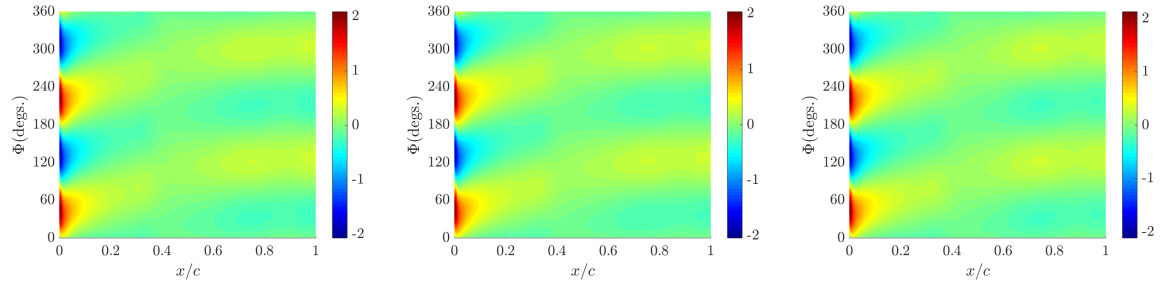

(a) Phase-averaged cycle 1-2 (b) Phase-averaged cycle 1-4 (c) Phase-averaged cycle 2-3

Figure 17: Comparison of upper surface -*cp* of DMD mode 3

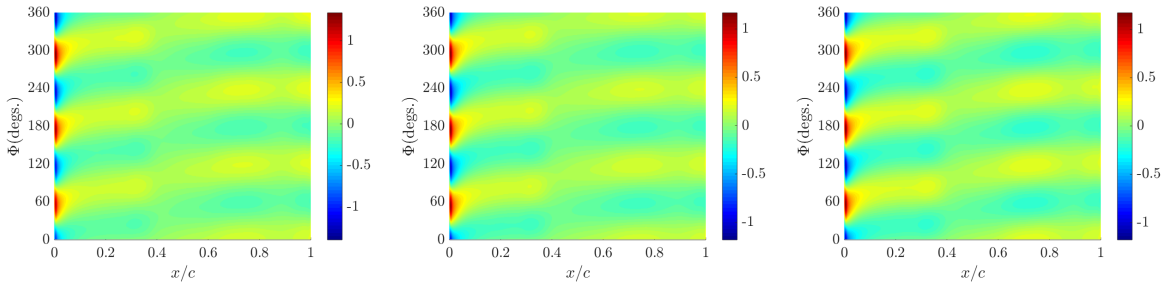

(a) Phase-averaged cycle 1-2 (b) Phase-averaged cycle 1-4 (c) Phase-averaged cycle 2-3

Figure 18: Comparison of upper surface -*cp* of DMD mode 4

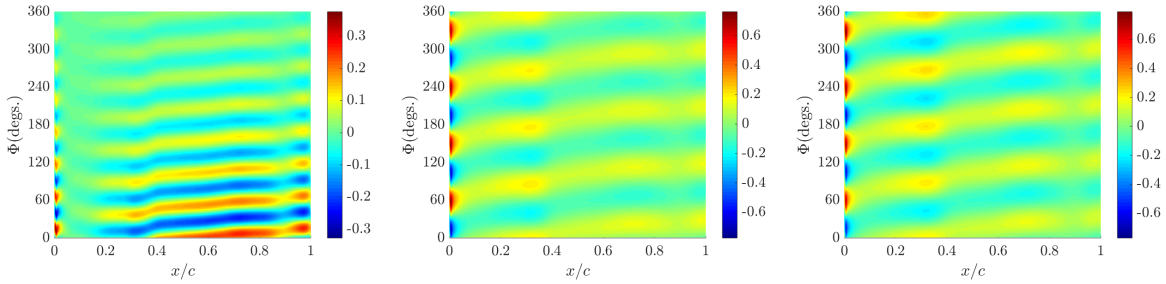

(a) Phase-averaged cycle 1-2 (b) Phase-averaged cycle 1-4 (c) Phase-averaged cycle 2-3

Figure 19: Comparison of upper surface -*cp* of DMD mode 5

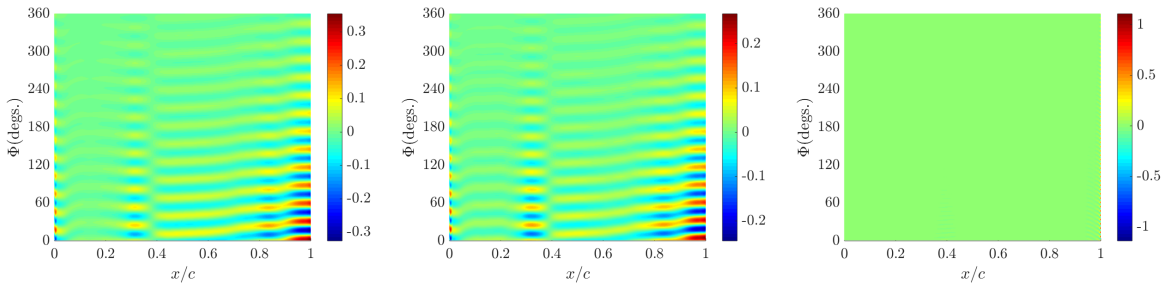

(a) Phase-averaged cycle 1-2 (b) Phase-averaged cycle 1-4 (c) Phase-averaged cycle 2-3

Figure 20: Comparison of upper surface -*cp* of DMD mode 6

5.3 Stability characteristics of DMD modes

Here we will discuss the stability of various DMD modes by investigating the real part of the modal eigenvalues. It is important to note that such modal stability is mostly an indication of the role of various modes in the flow separation as explained in Ref. [13]. Since this is a prescribed motion to the airfoil applied periodically over a cycle, the modal stability does not reflect the stability of the dynamical system.

The real part of the DMD eigenvalues for all the three cases are plotted in fig. 21 against the inverse of modal amplitude, for modes 2-6. Since the modes are ranked according to their modal amplitudes, the modal rank increases with the inverse of the modal amplitude. It is observed that for *PA cycle 1-4*, modes 3 and 4 show positive real part of the DMD eigenvalues indicating unstable modes. However, the positive real part is small for both the modes. Mode 2 has a very small negative real part of the eigenvalue, mode 5 has a moderate negative real part and mode 6 has a large negative real part. For *PA cycle 1-2*, mode 4 is unstable with a moderately large positive real part of the eigenvalue. Mode 2 and 3 show very small negative real part and modes 5 and 6 show a large negative real part. For *PA cycle 2-3*, modes 4 and 5 are unstable but mode 5 has a much larger positive real part than mode 4. Modes 2 and 3 has a small negative real part whereas mode 6 has a large negative real part. Overall we see that when phase-averaged over 4 cycles, some of the higher amplitude modes are unstable but with a small positive real part. However, both *PA cycle 1-2* and *PA cycle 2-3* have at least one unstable mode which has a moderately large real part of the eigenvalue. This is possibly because of phase-averaging retaining integral effects like aerodynamic forces, but not the modal features which vary in phase between the individual cycles. Although *PA cycle 1-2* and *PA cycle 2-3* are also phase-averaged, it is done over two cycles and still retains some of the effects of the cycle-to-cycle variations. However, phase-averaging over four cycles retains a much lower amount of individual cycle features like modal eigenvalues.

It is important to note that unstable DMD modes were also observed in a DMD analysis of deep dynamic stall in Ref. [13]. However, in that case, the positive the real part of the eigenvalues were much smaller than what is observed here for the light dynamic stall case, especially for *PA cycle 1-2* and *PA cycle 2-3*.

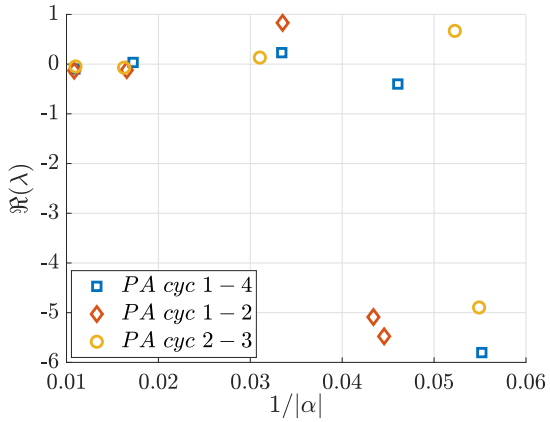

Figure 21: Comparison of modal damping (ranked according to $|\alpha|$) between DMD analysis of various phase-averaged pressure snapshots

6 CONCLUSIONS

In this study, a DMD analysis of the dynamic stall phenomena of a pitching NACA 0012 airfoil, occurring at high, turbulent Reynolds numbers and in the light stall regime, was presented. The CFD simulations for the test case were performed using DDES and the results obtained from DDES were first validated against experimental results obtained for a similar setup. The pitching moment predicted by the DDES showed negative cycle-averaged aerodynamic damping. The cp distribution predicted by the DDES showed large leading edge suction, the formation of the DSV at about 35% of the airfoil, movement of the DSV towards the trailing edge and eventual formation of the TEV. Significant cycle-to-cycle variations were observed in the phase and the amplitude of the LE suction, the suction coefficient associated with the DSV and the TEV, and in the cycle-averaged aerodynamic damping.

DMD analysis performed on the DDES pressure snapshots phase-averaged over four cycles showed a stationary mode that matched exactly with the time-averaged DDES pressure snapshots. The second DMD mode showed the frequency of the pitching motion and subsequent DMD modes were higher harmonics of the second DMD mode. The second DMD pressure mode showed a prominent leading edge suction region and another suction region coinciding with the path of the traveling DSV. The formation of the DSV could be identified in mode 4 at 35% of the chord. Modes 5, 6 and 7 showed the formation of the DSV at 35% of the chord as well as its movement towards the trailing edge much more clearly. Mode 6 also clearly showed the TEV which was not clearly evident in the other DMD modes. Although DMD Mode 6 is a much higher harmonic of mode 2, it was ranked ahead of some of the lower harmonics due to its much larger modal amplitude. This indicates the importance of the higher DMD modes, with relatively lower modal amplitude, in the important physical features of dynamic stall.

It was observed that a reduced-order model a model order of 99 (stationary mode + 49 DMD mode pairs) was required to reduce the peak $L2$ norm of the error between the reconstructed solution and DDES solution to 10%, especially during the phase of the DSV formation. Also, on increasing the number of DMD modes from $r = 49$ to $r = 99$, a significant improvement in the correlation between the reconstructed surface pressure distribution and its DDES counterparts was observed.

The cycle-averaged aerodynamic damping for both the DDES snapshots as well as the DMD pressure modes was obtained by computing the pitching moment at the quarter-chord via the pressure coefficients of surface grid points for the reduced computational domain. It was observed that DMD mode 2 was the most important contributor to the negative aerodynamic damping of the system. It had a negative cycle-averaged damping coefficient, with a relative value of 0.9958 to its counterpart computed for the DDES solution for the reduced domain.

DMD analysis was also performed on phase-averaged snapshots obtained from cycles 1 and 2 (*PA cycle 1-2*), and cycles 2 and 3 (*PA cycle 2-3*), and compared with that obtained earlier from the four cycles (*PA cycle 1-4*). It was observed that when the modes for the three cases were ranked based on their respective modal amplitudes, modes 1-3 of had same modal amplitudes for all the cases. For mode 4 onwards, somewhat different modal amplitudes for a specific mode number was observed for the three cases. Overall, the three cases show a similar pattern of modal amplitudes and modes 1-4 comprised most of the energy of the flow. Similar to *PA cycle 1-4* discussed earlier, several higher frequency modes for *PA cycle 1-2* and *PA cycle 2-3* had a larger modal amplitude than their lower frequency counterparts. For all the three cases, mode 1 is the stationary mode and the modes 2-4 are the same harmonics. However, mode

5 for *PA cycle 1-2* is not the third harmonic, unlike the other two cases. Similarly, mode 6 for *PA cycle 3-4* is a much higher harmonic than its counterparts for the other two cases. This shows the significantly different cycle-to-cycle modal participation taking place during dynamic stall. Such different pressure modes can be attributed to the differences in the surface pressure distribution from one cycle to another.

The stability characteristics of the DMD modes were also investigated by inspecting the real part of the eigenvalues of the DMD modes. Such modal stability is mostly indicative of the role of the DMD modes in flow separation. For the present case with prescribed periodic motion, such modal stability does not indicate the stability of the aerodynamic system. It was observed that for *PA cycle 1-4*, modes 3 and 4 were unstable modes, but with a small positive real part of the eigenvalue. For *PA cycle 1-2*, mode 4 was unstable with a moderately large positive real part of the eigenvalue. For *PA cycle 2-3*, modes 4 and 5 were unstable but mode 5 had a much larger positive real part than mode 4. Overall, it was observed that when phase-averaged over 4 cycles, the positive real parts of the eigenvalues of the unstable modes were much smaller than their counterparts obtained from both *PA cycle 1-2* and *PA cycle 2-3*. This is possibly because phase-averaging retains integral effects like aerodynamic forces, but not the modal characteristics which vary in phase between the individual cycles. *PA cycle 1-2* and *PA cycle 2-3* are also phase-averaged, but it is done over only 2 cycles and still retains some of the effects of the cycle-to-cycle variations. Phase-averaging over four cycles destroys the modal features that are present in the individual cycles.

Overall, the present study provided several key insights regarding the physics of the problem from a perspective of modal decomposition of a complex dynamic physical problem. Future work would comprise of further investigation of the problem to establish differences between the DMD modes for attached and separated flow, as well as dynamic stall in the light and deep stall regimes.

ACKNOWLEDGMENTS

During this research, the first author was supported in part at the Technion by a fellowship of the Israel Council for Higher Education. The authors also thank Yair Mor Yossef at the Israeli CFD Center for his help in the mesh development and useful insights regarding the DDES.

7 REFERENCES

[1] McCroskey, W. J. (1981). The phenomena of dynamic stall. *NASA Technical Report, NASA-TM-81264*.

[2] McCroskey, W. J., McAlister, K., Carr, L., et al. (1981). Dynamic stall on advanced airfoil sections. *Journal of the American Helicopter Society*, 26(3), 40–50.

[3] Ekaterinaris, J. A. and Platzer, M. F. (1998). Computational prediction of airfoil dynamic stall. *Progress in aerospace sciences*, 33(11-12), 759–846.

[4] Barakos, G. and Drikakis, D. (2003). Computational study of unsteady turbulent flows around oscillating and ramping aerofoils. *International journal for numerical methods in fluids*, 42(2), 163–186.

[5] Spentzos, A., Barakos, G. N., Badcock, K. J., et al. (2005). Investigation of three-dimensional dynamic stall using computational fluid dynamics. *AIAA journal*, 43(5), 1023–1033.

[6] Wang, S., Ingham, D. B., Ma, L., et al. (2010). Numerical investigations on dynamic stall of low reynolds number flow around oscillating airfoils. *Computers & Fluids*, 39(9), 1529–1541.

[7] Visbal, M. R. and Garmann, D. J. (2017). Analysis of dynamic stall on a pitching airfoil using high-fidelity large-eddy simulations. *AIAA Journal*, 46–63.

[8] Benton, S. and Visbal, M. (2019). The onset of dynamic stall at a high, transitional reynolds number. *Journal of Fluid Mechanics*, 861, 860–885.

[9] Chaouat, B. (2017). The state of the art of hybrid rans/les modeling for the simulation of turbulent flows. *Flow, Turbulence and Combustion*, 99(2), 279–327.

[10] Berkooz, G., Holmes, P., and Lumley, J. L. (1993). The proper orthogonal decomposition in the analysis of turbulent flows. *Annual review of fluid mechanics*, 25(1), 539–575.

[11] Schmid, P. J. (2010). Dynamic mode decomposition of numerical and experimental data. *Journal of fluid mechanics*, 656, 5–28.

[12] Mariappan, S., Gardner, A., Richter, K., et al. (2014). Analysis of dynamic stall using dynamic mode decomposition technique. *AIAA Journal*, 52(11), 2427–2439.

[13] Mohan, A. T., Gaitonde, D. V., and Visbal, M. R. (2016). Model reduction and analysis of deep dynamic stall on a plunging airfoil. *Computers & Fluids*, 129, 1–19.

[14] Dunne, R., Schmid, P., and McKeon, B. (2016). Analysis of flow timescales on a periodically pitching/surging airfoil. *AIAA Journal*, 30(3), 3421–3433.

[15] McCroskey, W. and Puccif, S. (1982). Viscous-inviscid interaction on oscillating airfoils in subsonic flow. *AIAA Journal*, 20(2), 167–174.

[16] Dindar, M., Kaynak, U., and Fujii, K. (1993). Nonequilibrium turbulence modeling study on light dynamic stall of a naca0012 airfoil. *Journal of aircraft*, 30(3), 304–308.

[17] Spalart, P. R., Deck, S., Shur, M. L., et al. (2006). A new version of detached-eddy simulation, resistant to ambiguous grid densities. *Theoretical and computational fluid dynamics*, 20(3), 181.

[18] Shur, M. L., Spalart, P. R., Strelets, M. K., et al. (2008). A hybrid rans-les approach with delayed-des and wall-modelled les capabilities. *International Journal of Heat and Fluid Flow*, 29(6), 1638–1649.

[19] Levy, Y. and Raveh, D. (2015). The eznss cfd code theoretical and user's manual.

[20] Mallik, W. and Raveh, D. (2019). Gust responses at high angles of attack. *AIAA Journal*. doi:10.2514/1.J057546.

[21] Martinat, G., Braza, M., Hoarau, Y., et al. (2008). Turbulence modelling of the flow past a pitching naca0012 airfoil at 105 and 106 reynolds numbers. *Journal of Fluids and Structures*, 24(8), 1294–1303.

[22] Wang, S., Ingham, D. B., Ma, L., et al. (2012). Turbulence modeling of deep dynamic stall at relatively low reynolds number. *Journal of Fluids and Structures*, 33, 191–209.

[23] Corke, T. C. and Thomas, F. O. (2015). Dynamic stall in pitching airfoils: aerodynamic damping and compressibility effects. *Annual Review of Fluid Mechanics*, 47, 479–505.

COPYRIGHT STATEMENT